OPEN ACCESS

Catalysis & Surface ARTICLE

The Innovation Energy

Synergistic pore-acidity engineering of hierarchical ZSM-5 for hydrogen-free upcycling of Polyethylene to C_8–C_{12} Methylated Aromatics

Bingyan Sun,[1] Bo Li,[1] Mate Marc,[1] Linjia Yin,[1] Qihui Song,[1] Xiaopeng Shi,[1] Dingran Wang,[1] Fawei Lin,[2,*] and Kaige Wang[1,*]

*Correspondence: linfawei@tju.edu.cn (F. L.); kaigewang@zju.edu.cn (K. W.)

Received: December 26, 2025; Accepted: March 10, 2026; Published Online: April 20, 2026; https://doi.org/10.59717/j.xinn-energy.2026.100155

GRAPHICAL ABSTRACT

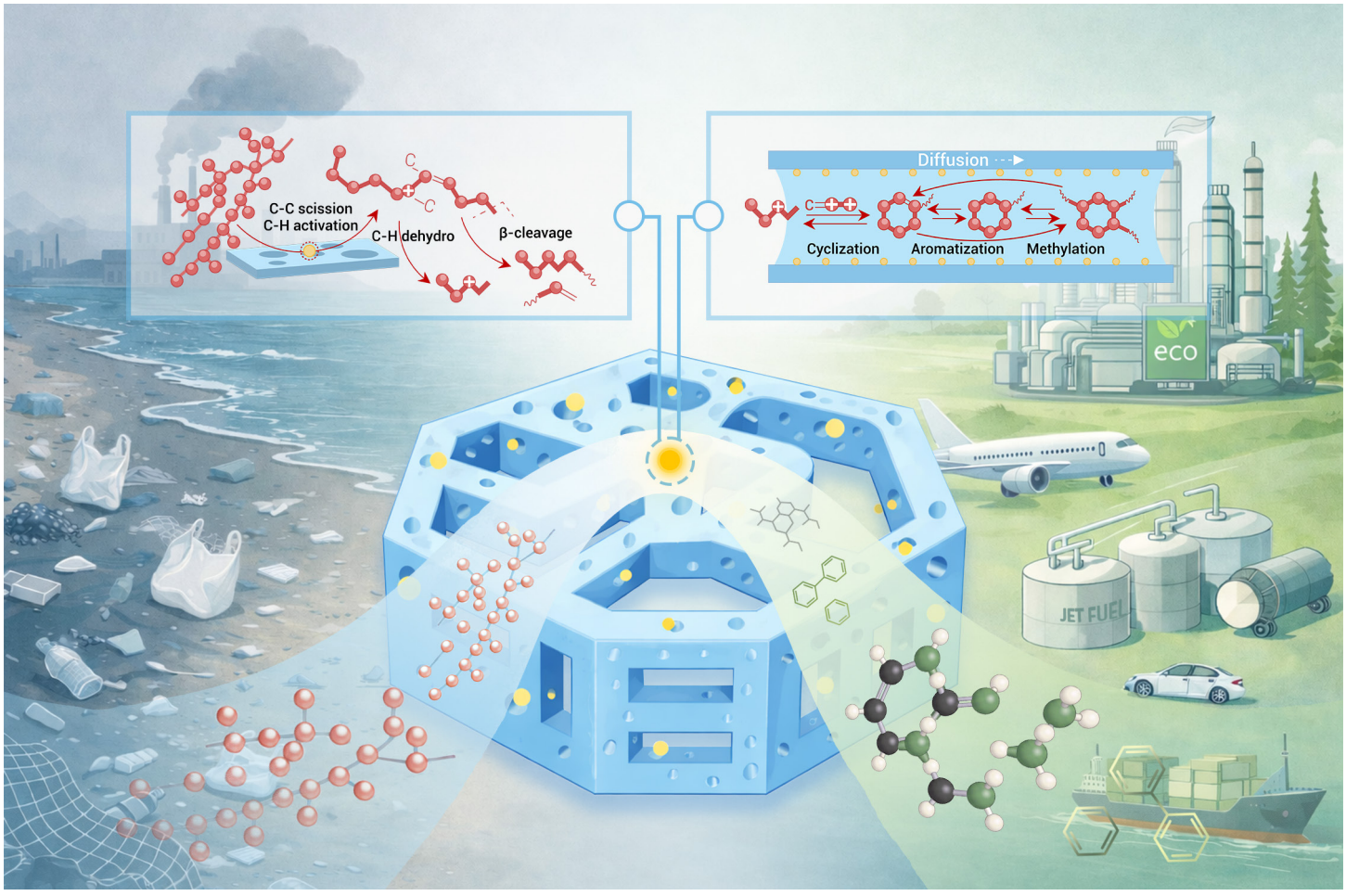

PUBLIC SUMMARY

- A pore-engineered ZSM-5 enables hydrogen-free conversion of polyethylene into valuable chemicals.
- Optimal pore–acidity synergy boosts conversion to 98.8% and aromatics yield to 37.4% at 280 °C.
- Mesopores enhance diffusion, speeding reactions and preventing over-cracking.
- The catalyst shows strong stability and works well for real-world plastic waste.
- Process cuts energy use and reduces emissions by over 55% vs fossil routes.

ARTICLE Catalysis & Surface

OPEN ACCESS

www.the-innovation.org/the-innovation-energy

Synergistic pore-acidity engineering of hierarchical ZSM-5 for hydrogen-free upcycling of Polyethylene to C_8–C_{12} Methylated Aromatics

Bingyan Sun,[1] Bo Li,[1] Mate Marc,[1] Linjia Yin,[1] Qihui Song,[1] Xiaopeng Shi,[1] Dingran Wang,[1] Fawei Lin,[2,*] and Kaige Wang[1,*]

[1]State Key Laboratory of Clean Energy Utilization, Zhejiang University, Hangzhou 310027, China

[2]School of Environmental Science and Engineering, Tianjin University, Tianjin 300072, China

*Correspondence: linfawei@tju.edu.cn (F. L.); kaigewang@zju.edu.cn (K. W.)

Received: December 26, 2025; Accepted: March 10, 2026; Published Online: April 20, 2026; https://doi.org/10.59717/j.xinn-energy.2026.100155

Citation: Sun B., Li B., Marc M., et al. (2026). Synergistic pore-acidity engineering of hierarchical ZSM-5 for hydrogen-free upcycling of Polyethylene to C_8–C_{12} Methylated Aromatics. *The Innovation Energy* **3**:100155.

Transforming polyethylene (PE) into high-value chemicals is often hindered by diffusion barriers. Here, we report a hydrogen-free strategy using pore-engineered hierarchical ZSM-5. By tuning desilication, we identified a critical pore–acidity synergy at an optimal V_{meso}/V_{micro} ratio of ~2.7 within this specific low Si/Al (25~50) framework. The optimal catalyst achieved near-complete conversion (98.8%) and an aromatic yield of 37.4% at a mild temperature of 280 °C. In-situ FTIR and molecular dynamics simulations reveal that this synergy facilitates a cascade reaction mechanism. The introduced mesoporosity enhances the effective diffusion coefficient of C_{10} intermediates by an order of magnitude (from 0.1 ×10^{-9} m^2s^{-1} to 2.2×10^{-9} m^2s^{-1}), thus enabling rapid turnover and suppressing over-cracking. The hierarchical catalyst (Hier-Z5-43) demonstrated exceptional stability and versatility for real-world plastic upcycling. Techno-economic and life cycle analyses confirm substantial advantages, reducing energy consumption by 10.9 MJ/kg and decreasing global warming potential by >55% compared to conventional fossil-based routes. This study highlights the importance of synergistically optimizing pore structure and acidity to enhance catalytic performance in polyolefin upcycling.

INTRODUCTION

PE, encompassing both low-density (LDPE) and high-density (HDPE) variants, constitutes over 60% of global plastic production.[1-3] Its pronounced chemical inertness impedes natural degradation, leading to persistent environmental accumulation and complicating end-of-life management.[4,5] Conventional disposal methods, such as landfilling and incineration, exacerbate microplastic pollution and greenhouse gas emissions, underscoring the urgent need for alternative recycling strategies.[6-8] As a polymer composed exclusively of carbon and hydrogen, PE constitutes a valuable feedstock for chemical valorization.[9-11] Its conversion into lower-carbon compounds offers a viable pathway toward establishing a circular economy.[12-14] In this context, chemical upcycling has emerged as a compelling approach to simultaneously enhance resource efficiency and generate liquid fuels and high-value chemicals from PE waste.[15-19]

PE and aromatics share similar carbon frameworks and energy content.[20-22] Catalytically converting PE waste into aromatics thus offers an attractive route to enhance carbon utilization and reduce dependence on fossil resources.[23-25] Methylated aromatics are vital industrial commodities, serving as versatile building blocks for chemicals and performance-enhancing additives for advanced fuels, such as sustainable aviation kerosene.[26-28] However, the primary approach for producing aromatics relies on naphtha reforming, typically requiring temperatures between 500 °C and 600 °C.[29] While catalytic pyrolysis of PE can achieve yields up to ~60 wt%, it also generally demands high reaction temperatures in the range of 500~700 °C.[30-32] Recently, milder strategies have gained attention. For instance, Scott et al. developed a novel approach employing a Pt/Al_2O_3 catalyst at 280 °C to convert PE into alkyl aromatics with 50 mol% selectivity, without requiring external hydrogen or solvents.[33] Leveraging similarly mild conditions, Chen et al. presented a methanol-facilitated cascaded upcycling process at 280 °C, achieving 97.8% LDPE conversion and an 87% increase in high-value C_9–C_{12} alkylbenzene mass yield.[34] Zhang et al. introduced a melting-catalysis approach using ZSM-5 zeolite to produce 50.6 wt% light aromatics from PE without H_2. Concurrently, Zeng et al. demonstrated that Ru/HZSM-5(300) efficiently upcycled HDPE under H_2- and solvent-free conditions, achieving 44.5 mol% aromatics.[35] Xiao et al. employed s-ZSM-5 and Zn/meso-ZSM-5 catalysts for the cascade conversion of PE into methylated aromatics, achieving complete PE conversion to C_{5+} products with a 60.1% yield.[27] These advances establish zeolites as effective catalysts for the hydrogen-free conversion of PE into aromatics, offering improved selectivity and stability.

Beyond the synergistic effect between metal sites and Brønsted acid sites,[36-40] the pore architecture of zeolites serves as a decisive factor in governing the catalytic microenvironment.

Confinement effects and van der Waals interactions within the framework dictate the diffusion of bulky polymer chains and intermediates, fundamentally shaping the reactivity and product distribution.[41-45] For medium-pore MFI zeolites, hierarchical structuring is typically advantageous, as evidenced by significantly reduced polyolefin degradation temperatures in thermogravimetric analyses compared to microporous analogues.[46] This enhancement is primarily attributed to improved accessibility and diffusion efficiency. Tsubota et al. demonstrated that initial PE cracking is initiated at the external surface and pore mouths, emphasizing that a threshold external surface area (~90 m^2/g) is essential for efficient primary deconstruction.[44] Once the chains are fragmented, the internal mesoporosity becomes critical for the egress of primary products. Specifically, Ru/MFI with tailored mesoporosity has been shown to expedite the diffusion of primary fragments, thereby mitigating secondary overcracking and enhancing liquid product yields by over 1.3-fold.[47] Similar trends have been observed in no added metal active sites systems; for instance, hierarchical MFI and FAU zeolites consistently outperform their microporous counterparts in conversion rates and branched-to-linear ratios, regardless of mesopore connectivity.[48,49] Furthermore, textural engineering via dealumination or desilication in Beta and Y zeolites has proven effective in optimizing gasoline-range product yields by maximizing active site exposure.[50,51] Recent efforts have further optimized this approach, such as using Bayesian optimization to precisely tailor ZSM-5 hierarchy for light olefin production[52] and developing amorphous-crystalline composites to decouple acidity from micropore confinement.[53] Both emphasize site accessibility for coke suppression and enhanced selectivity. Collectively, these advancements underscore that integrating mesopores is not merely a structural modification but a kinetic necessity to overcome mass transfer limitations in efficient plastic upcycling.

Incorporating mesopores into zeolites is a well-established strategy.[54-57] However, the systematic impact of mesopore geometry, particularly pore size, on its synergy with microporous acid sites remains largely unexplored for the hydrogen-free conversion of plastics into high-value aromatics. Herein, we report a comprehensive investigation into the pore–acidity relationship governing LDPE upcycling to methylated aromatics over pore-engineered hierarchical ZSM-5 catalysts. Our methodology involved the systematic synthesis of a catalyst suite to isolate the influence of the V_{meso}/V_{micro} ratio on conversion, high-value aromatic yield, and structural stability under H_2-free conditions. The optimal catalyst, Hier-Z5-43, featuring a V_{meso}/V_{micro} ratio of ~2.7 within this specific low Si/Al framework (25~50), achieved a liquid yield of 60.7% with 37.4% aromatic yield and exceptional stability over five cycles. Mechanistic analyses, supported by molecular dynamics simulations, definitively elucidated that the introduced mesoporosity accelerates the diffusion of bulky aromatic intermediates by an order of magnitude, confirming a synergy-driven cascade mechanism. Furthermore, a comprehensive life cycle assessment was performed, demonstrating that this process is energetically favorable and environmentally sustainable compared to fossil-based

production. This work not only presents a readily synthesized, high-performance hierarchical ZSM-5 catalyst but also deciphers the underlying pore–acidity synergy through the optimization of site accessibility and transport capacity. It provides fundamental insights into how mesopore size dictates the diffusion of key aromatic intermediates, establishing an effective and sustainable strategy for valorizing polyolefin waste into high-value chemicals.

MATERIALS AND METHODS

Chemicals and materials

Parent HZSM-5 zeolite (Si/Al = 50) was obtained from Nankai University Catalyst Co., Ltd. A diverse range of polyethylene feedstocks was employed: LDPE powder (Mw~110,000 melt index 25 g/10min (190 °C/2.16 kg), LDPE (average. Mw~4000 by GPC, average Mn~1700 by GPC), and HDPE (melt index: 6–9 g/10 min) were purchased from Sigma-Aldrich and Macklin. To evaluate practical applicability, real-world plastic waste, including LDPE gloves and LDPE/HDPE bottles, was sourced from Hangzhou Chentong Biochemical Technology Co., Ltd. These post-consumer plastics were mechanically shredded into 5 mm × 5 mm fragments using a paper cutting machine prior to use. Sodium hydroxide (NaOH, ≥ 96.0 %) and ammonium chloride (NH_4Cl, ≥ 99.5 %) were supplied by Sinopharm Chemical Reagent Co., Ltd. and used as received without further purification.

Synthesis of Hierarchical ZSM-5 catalysts

Hierarchical ZSM-5 was synthesized by desilication of pristine HZSM-5. Initially, the pristine ZSM-5 was calcined at 550 °C for 5 h in air to remove adsorbed moisture. Desilication was performed by mixing 5 g of ZSM-5 with 50 mL of NaOH solution (0.1, 0.2, or 0.4 M) at 80 °C under constant stirring (500 rpm) for varied durations (1, 3, or 5 h). The resulting samples were labeled Hier-Z5-XY, where X represents the NaOH concentration and Y denotes the treatment time. Post-treatment, the suspension was centrifuged, washed with ultrapure water until neutral pH, and dried at 80 °C overnight. To obtain the H-form, the samples underwent triple ion-exchange with 0.2 M NH_4Cl at 80 °C (2 h each), followed by vacuum filtration and rinsing with ≥500 mL of deionized water. Finally, the catalysts were calcined at 500 °C for 3 h (1 °C min^{-1}) in static air. Experimental screening (Table S1) revealed that excessive desilication at 0.6 M NaOH triggered framework collapse (Figure S1), reducing PE conversion to 20.5%, whereas insufficient treatment at 0.05 M failed to improve activity (33.6%). Consequently, the 0.1–0.4 M range was established to maximize accessibility while preserving the active crystalline framework.

Activity test and product analysis

PE upcycling was conducted in a 50 mL stainless steel autoclave (Anhui Kemi). Typically, 1.2 g of PE (or real plastic) and 0.2 g of catalyst were charged into the reactor. The vessel was purged with N_2 (1 MPa) for five cycles and subsequently pressurized to the target pressure (1–4 MPa) using N_2 containing 5 vol% CO_2 as an internal standard. The reactor was heated to the set temperature at 5 °C min^{-1}. Upon completion, the reactor was cooled to 20 °C and equilibrated for 15 min before product collection. The liquid products were recovered from the reactor using dichloromethane (DCM). The extraction efficiency was validated by multi-stage washing, where GC-MS analysis of the third washing cycle showed no detectable residues, confirming the exhaustive recovery of the products with the optimized DCM volume (8 mL). The gas inside the reactor was collected using an air bag. Gaseous products, with CO_2 used as an internal standard, were analyzed using a gas chromatography system (Agilent-8860) equipped with a flame ionization detector (FID) and thermal conductivity detector (TCD). CO_2, N_2 and H_2 were detected using TCD, while C_1–C_5 gas products were analyzed on an FID (detailed information in the Supporting Information). 8ml Dichloromethane was used as a solvent to extract products from the liquid-solid mixtures. The liquid-solid mixtures are separated through centrifugation. The liquid products that were collected and then analyzed using an Agilent GC-MS 8860 for gas chromatography-mass spectrometry analysis (detailed information in the Supporting Information). The solid residue was dried overnight at 80 °C and weighed to close the mass balance. The mass balance is used to calculate the yield of the collected gas, as shown in the following figure:

$$Y_g = \frac{M_g}{M_p}$$

$$Y_s = \frac{M_s}{M_p}$$

$$Y_l = 100\% - Y_g - Y_s$$

Where Y_g, Y_s and Y_l represent the yield of gas, solid and liquid respectively. M_g, M_s and M_p are the mass of gas, solid and LDPE powder, respectively.

Catalyst characterization

The crystallinity and phase purity of the catalysts were verified by X-ray diffraction (XRD, SmartLab SE-Rigaku) using Cu Kα radiation (λ = 1.541 Å) at 40 kV and 40 mA, with a scan speed of 5 °min^{-1}. Morphological features were captured via transmission electron microscopy (TEM, Tecnai 12) at 120 kV. Textural properties, including surface area and pore size distribution, were determined by N_2 physisorption at 77 K (Autosorb-iQ3). The V_{micro}, S_{micro}, and $S_{external}$ were calculated using the t-plot method (Harkins-Jura model), while V_{meso} and S_{meso} were derived from the BJH adsorption branch. Total acidity was evaluated by NH_3 temperature-programmed desorption (NH_3-TPD, AutoChemII2920) from 100 to 600 °C (10 °C min^{-1}). The nature of acid sites (Brønsted vs. Lewis) was identified by pyridine-adsorbed Fourier transform infrared spectroscopy (Py-FTIR, Nicolet iS50). Samples were evacuated at 400 °C for 30 min before pyridine saturation; spectra were subsequently recorded at 150, 300, and 350 °C. The concentrations of B and L acid sites were quantified by integrating the bands at 1540 cm^{-1} and 1450 cm^{-1}, respectively. Carbonaceous deposits and polymer residues were analyzed via thermal gravimetric analysis (TGA) from 50 to 800 °C (10 °C min^{-1}) and differential scanning calorimetry (DSC, DSC 2500) from 30 to 200 °C.

Details regarding the synthesis of modified catalysts (Hier-Z5-43-TPA, Hier-Z5-43-DAl, and Hier-Z5-43@SiO_2), in situ FTIR protocols, MD simulation parameters, and the comprehensive TEA and LCA methodologies are provided in the Supporting Information (SI).

RESULTS AND DISCUSSION

Engineering hierarchical porosity and structural characterization

To systematically investigate the pore-acidity synergy, we synthesized a gradient series of hierarchical ZSM-5 catalysts (Hier-Z5-11 to -45) and designed a suite of control samples (Hier-Z5-43-TPA, -DAl, @SiO_2). This design allows us to decouple the individual contributions of mesopore accessibility and acid site distribution to the upcycling process.

Structural characterization first confirmed the controlled evolution of hierarchical porosity. XRD patterns (Figure 1A) confirms the preservation of the MFI framework across all samples, while the progressive decline in crystallinity from ZSM-5 to Hier-Z5-45 reflects the gradient-controlled etching of the framework. Quantitative analysis via XRD and ICP-OES (Table S2) confirms that all hierarchical catalysts maintain high relative crystallinity (>85%) despite the systematic decrease in bulk Si/Al ratio (from 50 to 23), demonstrating the preservation of the MFI framework during controlled desilication. Furthermore,[27]Al and [29]Si MAS NMR spectra (Figure S2) verify the preservation of tetrahedral framework aluminum and the structural integrity of the Si(0Al) environments, confirming that desilication proceeds without significant framework amorphization. N_2 adsorption–desorption isotherms (Figure 1B) further delineates the textual evolution, i.e., the materials transitioned from a Type I isotherm (purely microporous) to a Type IV isotherm with distinct H4-type hysteresis loops, providing unambiguous evidence for successful mesopore integration.[48,58] Pore size distribution curves (Figure 1C) and quantitative data (Table 1) systematically capture this progression, i.e., the ratio of meso-to-micropore volume (V_{meso}/V_{micro}) increased monotonically from 0.54 (pristine ZSM-5) to 3.44 (Hier-Z5-45). This textural shift was accompanied by a targeted expansion of the average pore size from 3.1 to 5.3 nm, providing the necessary space for large molecule diffusion. TEM imaging (Figure 1D) provided direct visualization, with Hier-Z5-43 and -45 crystals exhibiting abundant intracrystalline voids, corroborating the physisorption data.

The control samples achieved manipulation of specific structural variables.

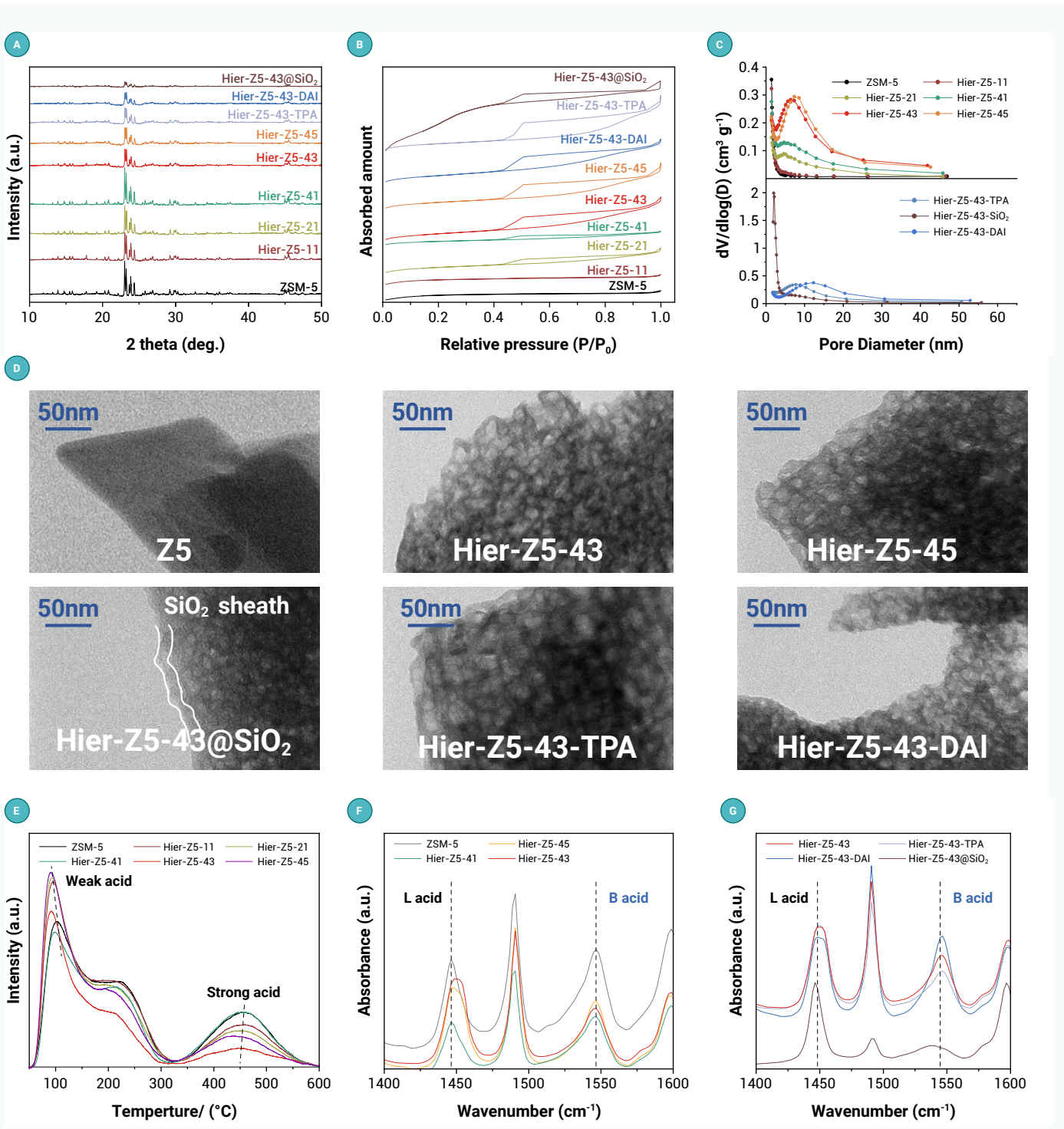

Figure 1. Structural and acidic characterization of the catalysts (A) Powder XRD patterns. (B) N_2 adsorption–desorption isotherms. (C) Pore size distribution curves. (D) TEM images. (E) NH_3-TPD profiles. (F) and (G) Py-IR spectra of the desilicated series.

The significantly constricted hysteresis loop and TEM of Hier-Z5-43@SiO_2 confirmed effective pore entrance blockage by the silica shell. In Hier-Z5-43-TPA, mesopore accessibility was reduced due to template residue, while Hier-Z5-43-DAI displayed a more fragmented framework. Collectively, these samples allow us to systematically decouple the individual contributions of pore accessibility and acid site distribution in the subsequent catalysis.

Evolution and decoupling of acidic properties

With well-defined pore architectures established, we next analyzed the evolution of acidity. NH_3-TPD profiles (Figure 1E & Table 1) indicate that the total acid density of the desilicated series remained relatively robust (0.70–0.79 mmol g^{-1}), demonstrating that the hierarchical restructuring did not cause a net, massive loss of acid-generating centers. However, pyridine-adsorbed FTIR (Figure 1F & G) revealed a significant change in the acid site quality. The concentration of accessible Brønsted acid sites (BAS) followed a downward trend with increasing desilication intensity (decreasing from 442 to 248 μmol g^{-1}), primarily due to concomitant framework dealumination. This systematic reduction establishes a quantifiable acidity gradient that mirrors the evolution of porosity. To further evaluate the quality of the

Table 1. Textural properties and acidity of ZSM-5, hierarchical ZSM-5, and modified catalysts.

Catalysts	Surface area (m^2 g^{-1})	[a]V_{micro} (cm^3/g)	[b]V_{meso} (cm^3/g)	V_{meso}/V_{micro}	[c]Density of acid sites (mmol g-1)	[d]Acidity (μmol/g)	
						Brønsted	Lewis
Z5	412	0.13	0.07	0.54	0.77	442	181
Hier-Z5-11	392	0.12	0.07	0.58	0.79	373	271
Hier-Z5-21	355	0.11	0.09	0.82	0.78	240	131
Hier-Z5-41	411	0.11	0.15	1.36	0.72	219	102
Hier-Z5-43	427	0.11	0.30	2.73	0.71	226	205
Hier-Z5-45	435	0.09	0.31	3.44	0.70	248	196
Hier-Z5-43-TPA	439	0.10	0.30	3.00	0.55	167	207
Hier-Z5-43-SiO_2	901	0.20	0.48	2.40	0.27	74	153
Hier-Z5-43-Dal	405	0.10	0.32	3.20	0.61	332	198

[a] t-plot method. [b] BJH adsorption isotherma. [c] Determined via NH_3-TPD [d] Determined via Py-IR.

remaining acid sites, the distribution of weak (150–300 °C) and strong (>350 °C) BAS was quantified via Py-IR (Table S3 & Figure S3). Although the absolute concentration of all acid sites decreased post-desilication, the relative proportion of strong BAS exhibited a distinct upward trend, increasing from 33.4% in parent Z5 to 40.5% in Hier-Z5-43. This suggests that the alkaline treatment preferentially removes unstable weak acid sites often associated with silanol defects, while preserving the robust framework BAS on the newly formed mesopore walls to generate a more efficient catalytic interface. Critically, the control samples successfully decoupled porosity from acidity. Hier-Z5-43-DAl, subjected to an additional acid wash, exhibited a higher concentration of accessible BAS (332 μmol g^{-1}) than its precursor Hier-Z5-43 (226 μmol g^{-1}). This phenomenon indicated that the HCl treatment removed extra-framework aluminum debris, thereby enhancing the accessibility of internal BAS by unclogging micropore channels. Conversely, Hier-Z5-43-TPA showed a markedly lower BAS concentration (167 μmol g^{-1}) due to physical blockage by the template, while Hier-Z5-43@SiO_2 displayed nearly negligible acidity (74 μmol g^{-1}), confirming the effective isolation of active sites by the core-shell architecture.

In summary, this section establishes a clear gradient in porosity from microporous to hierarchical structures via the main catalyst series. Furthermore, the strategic use of control samples effectively isolates the effects of "pore accessibility" and "acid site distribution." This foundational work sets the stage for directly probing how the specific synergy between pore architecture and acid properties governs the catalytic upcycling of PE.

Catalytic performance: Unveiling the pore-acidity synergy

Optimal Performance and the Critical Role of Mesopores. The catalytic efficacy of the hierarchical series was first evaluated for LDPE upcycling (Figure 2A). Parent ZSM-5 exhibited limited activity (42.5% conversion, 33.9% liquid yield) due to severe diffusion constraints within its purely microporous framework. In contrast, the introduction of mesoporosity triggered a significant performance leap, with Hier-Z5-43 (optimal V_{meso}/V_{micro}~ 2.7) emerging as the premier catalyst by achieving near-complete conversion (98.8%) and a peak liquid yield (60.7%). This high efficiency is supported by GC-MS and GC analyses (Figures S4 & S5), which confirm a high-quality liquid fraction and a specific gas-phase distribution that is representative of the entire series (Table S4). Furthermore, quantitative hydrogen analysis (Table S5) shows that Hier-Z5-43 generates 0.34 mmol of H_2, over twice that of ZSM-5 (0.16 mmol), providing direct stoichiometric evidence for enhanced dehydrocyclization. This increased evolution, coupled with the formation of light alkanes via hydrogen transfer, confirms the accelerated aromatic turnover enabled by the hierarchical structure. Excessive desilication (Hier-Z5-45, V_{meso}/V_{micro} ~3.4), however, induced a structural trade-off: while its over-expanded mesopores facilitate mass transport, they simultaneously promote non-selective secondary cracking of intermediates into light gases.

Decoupling Pore Accessibility and Acidity via Control Experiments. The precisely engineered control samples provided direct evidence for the distinct roles of pore accessibility and acid sites (Figure 2A). Blocking mesopores (Hier-Z5-43-TPA) caused a significant drop in conversion (78.1%), underscoring that open transport channels are essential for polymer chain access. Enhancing acid site accessibility without altering mesoporosity (Hier-Z5-43-DAl) led to complete conversion (99.1%) but with the highest gas yield (47.8%), signifying over-cracking at highly exposed strong acid sites. Most conclusively, physically insulating the active surface (Hier-Z5-43@SiO_2) resulted in the lowest activity (31.3%), definitively proving that the external surface and mesopore entrances are the primary active zones for initial polymer cleavage.[59,60] Detailed product distributions for these probes are provided in Figure S6 & S7 and Table S4.

Maximizing C_8–C_{12} Aromatics Yield. The yield of desired C_8–C_{12} aromatics, a key metric for upcycling, mirrored the conversion trend, peaking at 37.4% for Hier-Z5-43 (Figure 2B). Detailed product analysis (Figure 2D) confirms that Hier-Z5-43 shifts the liquid product slate from a complex mixture of light hydrocarbons (ZSM-5) toward valuable methylated aromatics, predominantly in the C_9–C_{10} range. Selectivity toward methylated aromatics soared to 61.5% (Figure 2E), as corroborated by ^{1}H NMR resonances of methyl-substituted benzenes (Figure 2F). Complementary DSC analysis (Figure 2G) showed a marked decrease in residue melting points (~80 °C vs. 110 °C for LDPE), signifying efficient depolymerization. Systematic condition optimization identified 280 °C and 3 MPa as the ideal parameters (Figure 2B & C), with higher temperatures and pressures leading to secondary cracking or reduced selectivity (Figures S8–S11).

Quantifying the Pore–Acidity Synergy. To establish a predictive framework, we established a quantitative correlation between the aromatic yield and the two key descriptors: V_{meso}/V_{micro} ratio and BAS density (Figure 3). The aromatic yield exhibits a threshold behavior (Figure 3A), rising sharply once the V_{meso}/V_{micro} ratio exceeds 1.0, marking the transition from a diffusion-limited to an accessibility-enhanced regime. The correlation with BAS density (Figure 3B) follows a volcanic distribution, identifying "accessible acidity" rather than total acidity as the primary performance descriptor. This intrinsic acidity dependence was further validated by a series of catalysts with Si/Al ratios from 50 to 600 (Table S6). Even when the V_{meso}/V_{micro} ratio was maintained near the optimal ~2.7, the aromatic yield declined significantly with decreasing acid density, particularly in high-silica samples where the scarcity of framework Al hindered both structural modification and catalytic initiation. This synergy is visualized in a 2D functional map (Figure 3C), which delineates three regimes: (i) a diffusion-restricted zone (high BAS, low V_{meso}), (ii) an acid-deficient zone (low BAS, high V_{meso}), and (iii) an optimal zone where moderate, accessible BAS pairs with sufficient mesoporosity. Hier-Z5-43 resides precisely in this optimal zone, achieving maximal aromatic yield by synergistically aligning molecular transport with acid-catalyzed aromatization.

Finally, a comprehensive benchmarking against recently reported ZSM-5-based catalysts (2023–2025) was conducted (Figure 2H & Table S7). Hier-Z5-

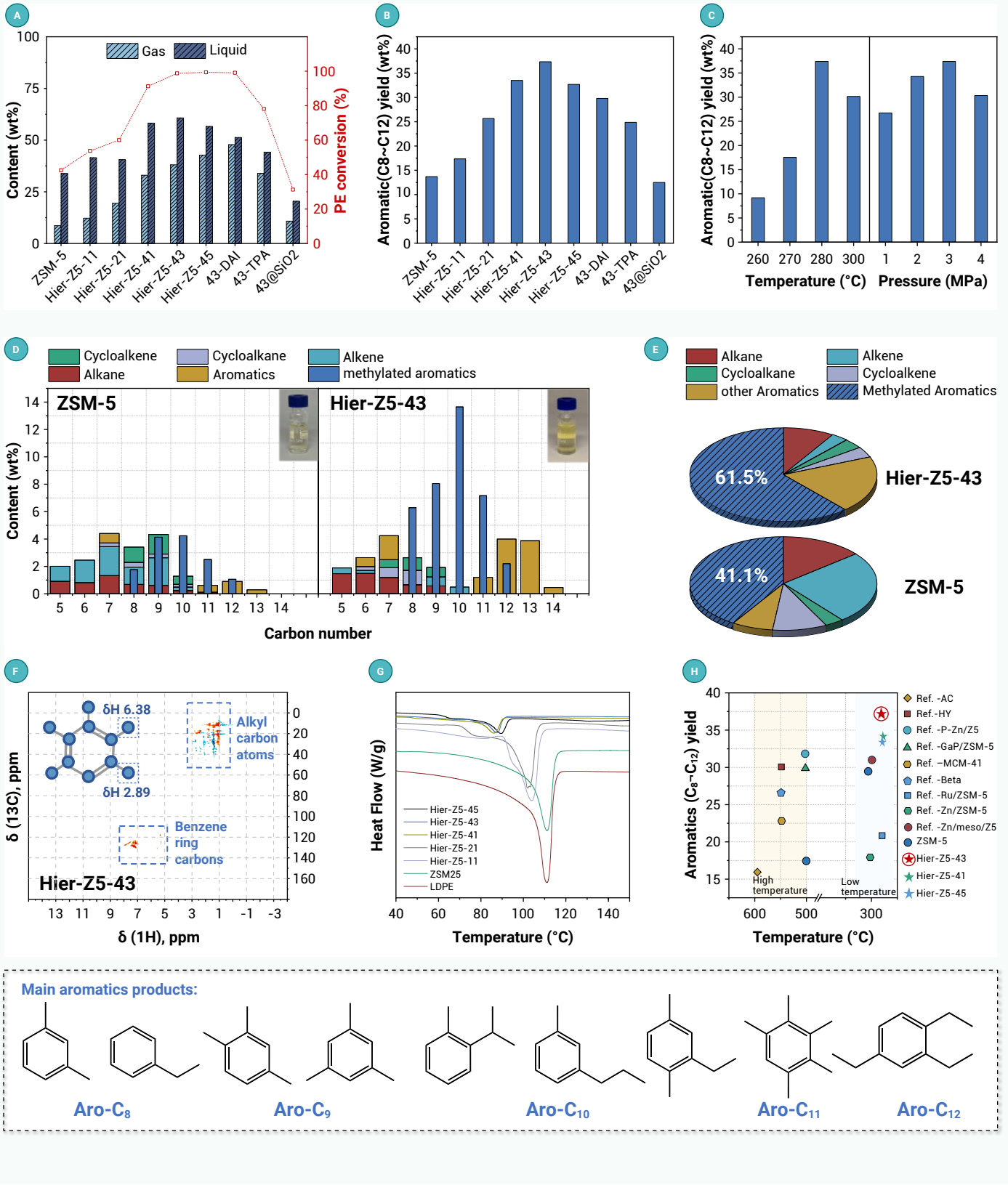

Figure 2. (A) Screening of catalytic performance (PE conversion and product distribution) over parent ZSM-5 and the series of pore-engineered Hier-Z5 catalysts (Reaction conditions: 280 °C,3 MPa N_2,1h). (B) Yield of C_8–C_{12} aromatics as a function of desilication intensity. (C) Optimization of reaction temperature and pressure over Hier-Z5-43. (D) Carbon number distribution and (E) selectivity of liquid products compared between ZSM-5 and Hier-Z5-43. (F) ^{1}H NMR spectra of liquid products. (G) DSC curves of post-reaction residues. (H) Comparison of C_8–C_{12} aromatic yield and reaction temperature with literature benchmarks.

43 delivered a superior C_8–C_{12} aromatic yield of 37.4%, significantly outperforming the unmodified ZSM-5 (23.7%) and even exceeding several state-of-the-art metal-loaded systems (e.g., Ru, Zn, or Ga-doped ZSM-5) that typically require reaction temperatures 200–300 °C higher. This comparison

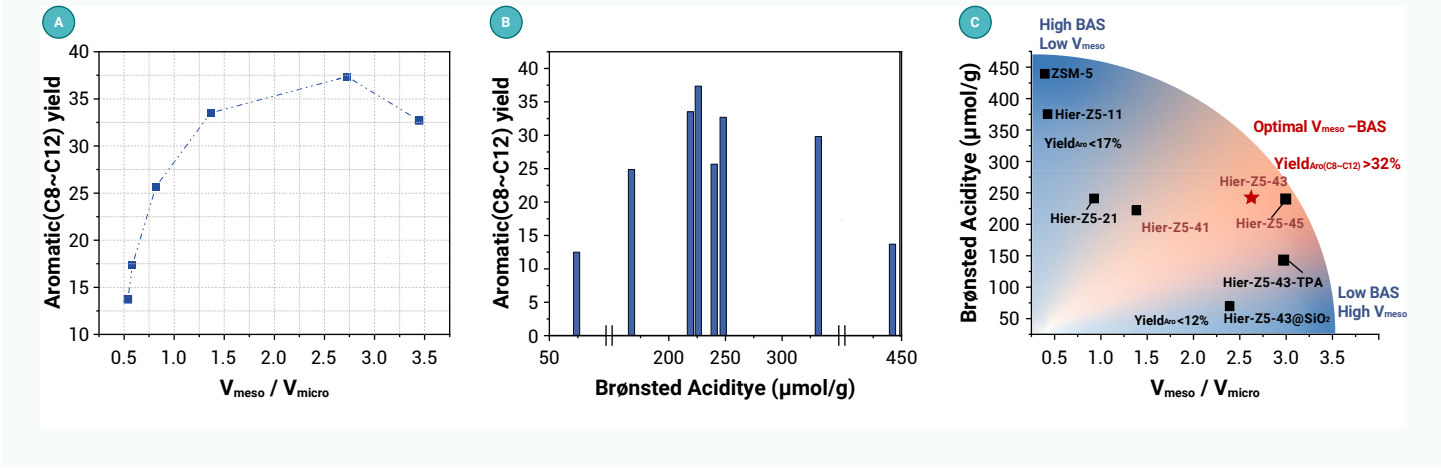

Figure 3. Quantitative correlation between structural properties and catalytic performance (A) Relationship between V_{meso}/V_{micro} ratio and C_8–C_{12} aromatic yield. (B) Correlation of Brønsted acid site (BAS) density with aromatic yield. (C) 2D synergistic map of V_{meso}/V_{micro} and BAS density for aromatic production, categorized into diffusion-restricted, acid-deficient, and moderate V_{meso}–BAS balance regimes.

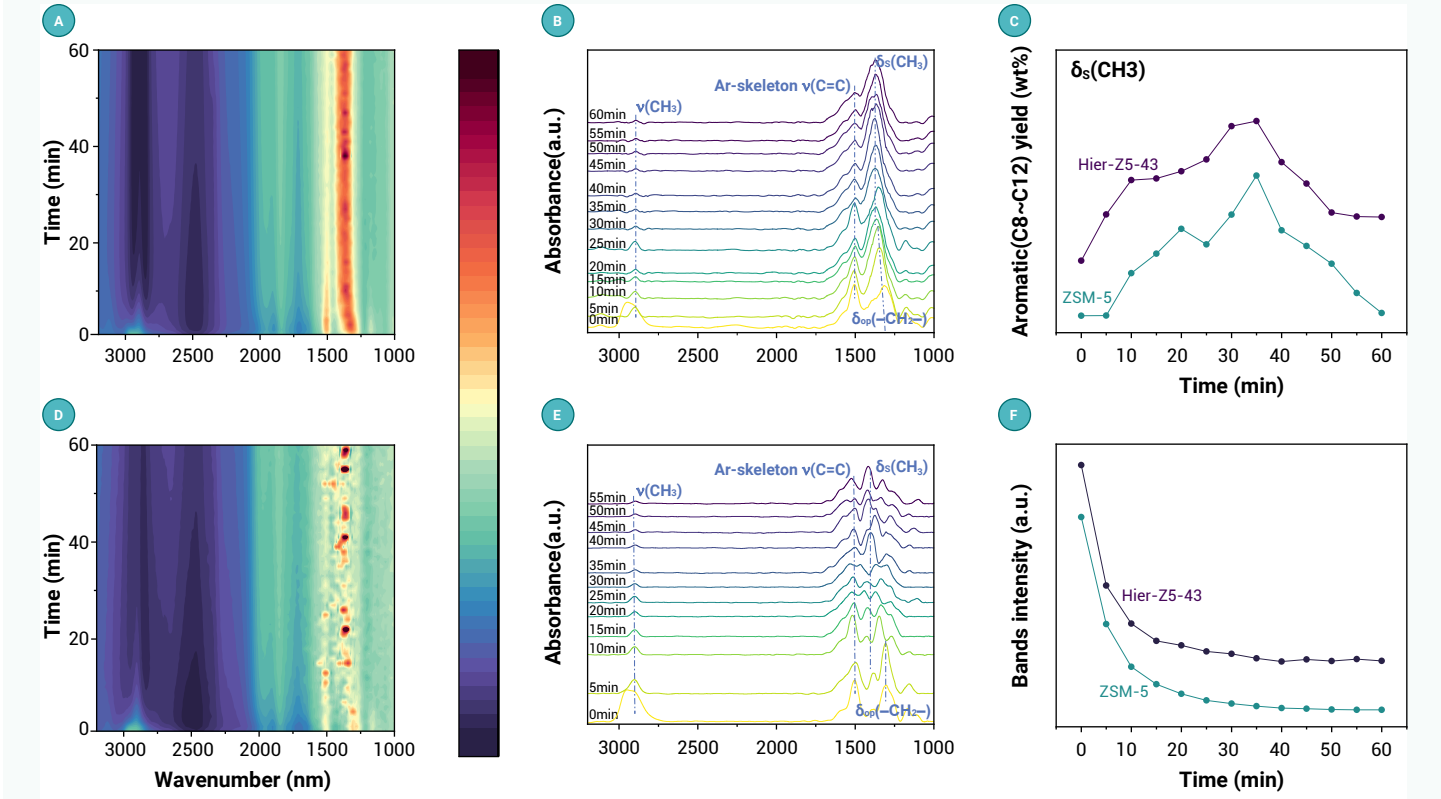

Figure 4. (A) 2D correlation/contour map of in-situ IR spectra over Hier-Z5-43 (visualizing band evolution with time). (B) Time-series in-situ IR spectra over Hier-Z5-43 (0–60 min), highlighting ν(CH$_3$) (~2897 cm^{-1}), aromatic skeleton ν(C=C) (~1501 cm^{-1}), δs(CH$_3$) (~1369 cm^{-1}), and δop(–CH$_2$–) (~1319 cm^{-1}). (C) Kinetics of δs(CH$_3$) (~1369 cm^{-1}) intensity vs. time: comparison between ZSM-5 and Hier-Z5-43. (D) 2D correlation/contour map of in-situ IR spectra over ZSM-5. (E) Time-series in-situ IR spectra over ZSM-5 (0–60 min), assigned as in panel. (F) Kinetics of ν(CH$_3$) (~2897 cm^{-1}) intensity vs. time: comparison between ZSM-5 and Hier-Z5-43.

highlights the potential of our pore-acidity synergy strategy for enabling energy-efficient plastic upcycling.

Mechanistic insights from in-situ IR and molecular simulations

Accelerated intermediate turnover probed by time-resolved in-situ IR. To gain molecular-level kinetic insight, time-resolved in-situ FTIR was performed to monitor the evolution of intermediate species at the PE–catalyst interface (Figure 4A). We specifically tracked the δs(CH$_3$) (~1369 cm^{-1}) and ν(CH$_3$) (~2897 cm^{-1}) features, which serve as fingerprints for the formation and subsequent turnover of methyl-substituted aromatic intermediates.[61-64] As shown in Figure 4C & F, Hier-Z5-43 exhibits a significant kinetic advantage over the parent ZSM-5. The intensity of these methyl-related bands increased steeply on Hier-Z5-43, reaching a maximum at 35 min, followed by a distinct decline. This "rise-and-fall" behavior indicates that aromatic inter-

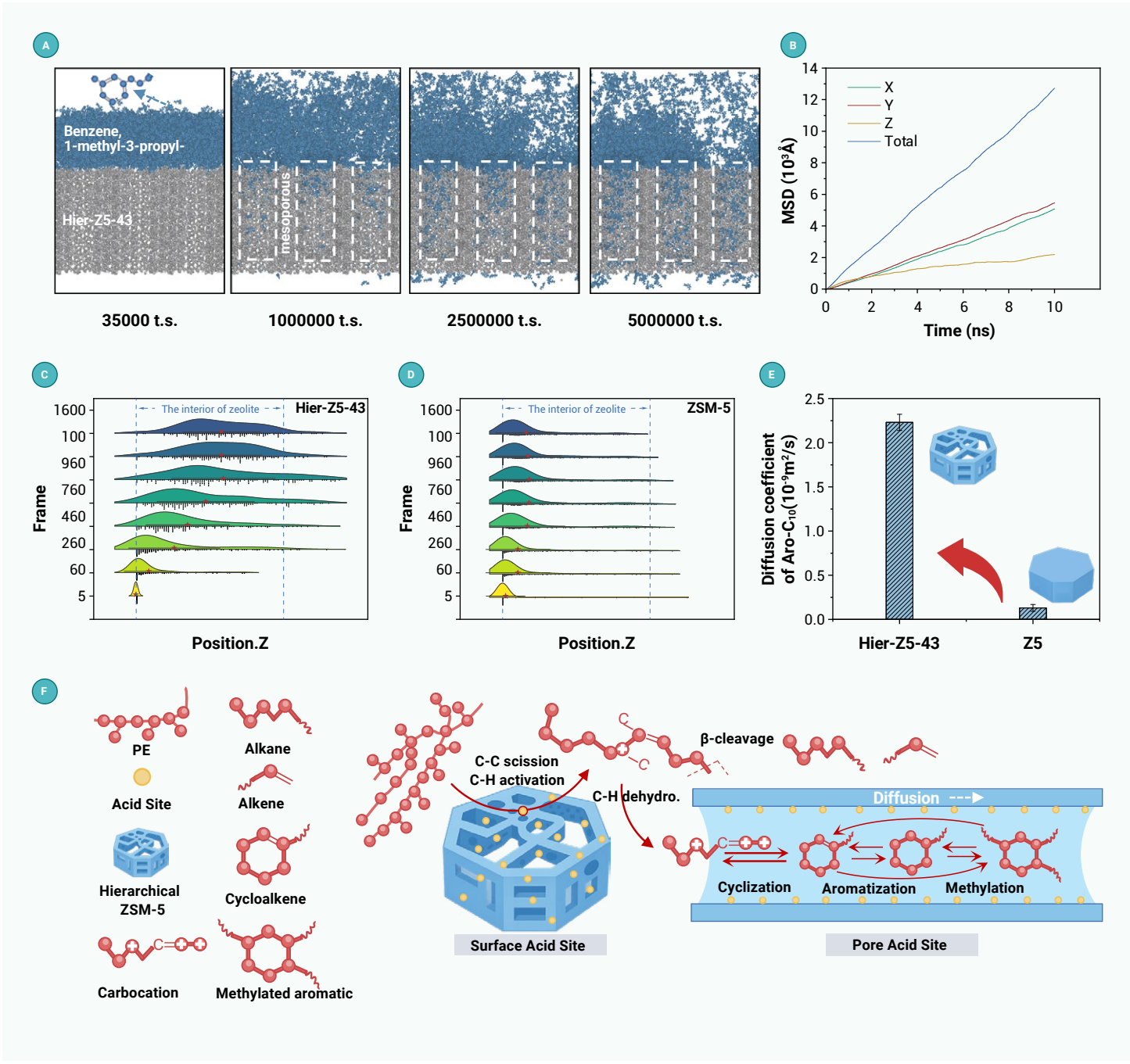

Figure 5. Molecular simulations reveal mesopore-enabled diffusion and a meso–micro cascade to methylated aromatics (A) Snapshots of 3,000 benzene, 1-methyl-3-propyl molecules diffusing in the mesoporous model (t = 35k, 1,000k, 2,500k, 5,000k timesteps; total 10 ns), showing progressive ingress and through-pore transport (mesopore diameter ~4.9 nm).(B) MSD curves (X, Y, Z and total) for Aro-C_{10} in the mesoporous model; the linear regime supports diffusivity extraction (slope/6).(C) Spatial distributions (counts vs. distance; 0–70 = in-pore region) at selected frames for the mesoporous model, evidencing increasing internal occupancy over time.(D) Spatial distributions under identical conditions for the microporous ZSM-5 model, showing negligible ingress.(E) Diffusion coefficients of Aro-C_{10}: 2.2 × 10^{-9} m^2 s^{-1} (mesoporous) vs 0.11 × 10^{-9} m^2 s^{-1} (microporous).(F) Proposed mesopore-assisted pathway

mediates were rapidly generated and subsequently consumed or desorbed as final liquid products. In contrast, ZSM-5 showed a much slower accumulation rate and failed to show a significant turnover within the same timeframe, suggesting that species were trapped within the purely microporous network.

This kinetic discrepancy directly correlates with the pore-acidity synergy established in Figure 3C. The optimized V_{meso}/V_{micro} ratio in Hier-Z5-43 provides a dual benefit: (i) accelerated ingress, where the shortened diffusion path allows bulky PE fragments to rapidly access internal Brønsted acid sites (BAS) for aromatization; and (ii) facilitated egress, where the open mesoporous architecture prevents "over-processing" by enabling C_8–C_{12} intermediates to escape the acidic environment before undergoing non-selective secondary cracking or coke formation.

Molecular dynamics simulation: quantifying enhanced diffusion. To rationalize the accelerated kinetic turnover observed by in-situ IR, MD simulations were performed using 1-methyl-3-propylbenzene (Aro-C_{10}) as a representative bulky intermediate. Models for Hier-Z5-43 (Figure S12) and ZSM-5 (Figure S13) were constructed to reflect experimental pore dimensions, specifically matching the optimal mesopore size of ~4.9 nm (Table S8).

Molecular trajectory and distribution analysis (Figure 5A&B and Figure S14) provides immediate visual evidence of the diffusion mechanism. In Hier-Z5-43, Aro-C_{10} molecules demonstrated rapid ingress and substantial through-pore transport, transitioning from the crystal face to the entire 4.9 nm

mesochannel interior. In stark contrast, ZSM-5 showed negligible displacement, with molecules remaining sterically confined at the crystal exterior, confirming the severe diffusion bottlenecks created by narrow MFI micropores.[65]

Quantitative proof of this mass transport enhancement was provided by Mean Square Displacement (MSD) analysis (Figure 5B & E). In Hier-Z5-43 (Figure 5C), Aro-C_{10} molecules quickly transitioned from initial accumulation at the crystal face to populating the entire ~4.9 nm mesochannel interior, with the distribution center shifting towards the crystal center over time. Conversely, the ZSM-5 model (Figure 5D) showed negligible ingress, with molecules remaining confined primarily to the initial side of the crystal. Quantitative proof for enhanced mass transport was provided by Mean Square Displacement (MSD) analysis (Figure 5B). The effective diffusion coefficient (D_{eff}) of Aro-C_{10} was calculated as 2.2×10^{-9} m^2s^{-1} in the mesoporous model, which is an order-of-magnitude enhancement compared to 0.11×10^{-9} m^2s^{-1} in the ZSM-5 model (Figure 5E). This computational evidence confirms that the hierarchical architecture successfully overcomes mass transfer limitations for bulky aromatic products.[65]

Synergistic Mechanism Facilitated by Pore–Acidity Balancing. Based on the in-situ IR and MD evidence, we propose a pore-acidity synergistic mechanism (Figure 5F) that governs the efficient conversion of LDPE. This mechanism represents the molecular-level manifestation of the optimal balance between mass transport and intrinsic acidity. The conversion proceeds through a series of coordinated steps: (i) surface-initiated depolymerization: LDPE chains, softened on the catalyst surface, undergo initial β-scission and hydride/β-H transfer at accessible Brønsted acid sites to generate reactive fragments; (ii) cooperative aromatization: These fragments are rapidly processed into aromatic intermediates within the cooperative meso–micro domains, where the hierarchical structure ensures maximum site utilization; (iii) Synergistic Alkylation: Interaction with C_1–C_3 olefin pools yields the final bulky C_8–C_{12} methylated aromatics. The quantitative acid distribution (Table S3) provides further insight into the reaction cascade. The increased proportion of strong BAS in Hier-Z5-43 is critical for aromatization, providing the requisite catalytic intensity for the dehydrocyclization of olefinic fragments. Unlike parent Z5, where a high density of strong acid sites drives non-selective deep cracking to light gases, the moderated density of strong BAS in Hier-Z5-43 enables precise catalysis, favoring aromatic ring formation and effectively suppressing secondary over-cracking. This spatial synergy dramatically curtails the residence time of reactive intermediates, effectively partitioning the carbon flux toward high-value methylated aromatics. By decoupling the residence time from the intrinsic reaction rate, the hierarchical structure bypasses the thermodynamic tendency toward non-selective over-cracking and coke formation that plagues purely microporous ZSM-5.

Structural robustness, practical versatility, and system-level sustainability

Building upon the identified pore-acidity synergy, we evaluated the structural robustness of the optimal catalyst, its efficacy in real-world applications, and the overall sustainability of the proposed upcycling process.

Thermal analysis and operational stability. The intrinsic activity advantage of Hier-Z5-43, rooted in its optimized structure, was first confirmed by TG /DTG analysis (Figure 6A & B). Under isothermal conditions at 280 °C, an LDPE/Hier-Z5-43 mixture achieved ~60% conversion within 1 hour, vastly outperforming the parent ZSM-5 (~10% conversion). The distinct decomposition rate peak observed exclusively for Hier-Z5-43 (Figure 6B) provides kinetic evidence of its superior activity at mild temperatures.

More importantly, the catalyst demonstrated exceptional operational stability over five consecutive reaction-regeneration cycles (Figure 6C & D). The average liquid yield remained remarkably stable at ~59.6 wt%, and the yield of high-value C_8–C_{12} aromatics persisted between 32.5% and 34.3%. This remarkable stability underscores the structural robustness of the hierarchical framework, confirming that the engineered porosity and active sites are not compromised by repeated regeneration. The efficacy of the in-situ calcination regeneration (550 °C, air) was confirmed by digital photographs (Figure S15) and textural analysis (Table S9). These characterizations revealed near-complete recovery of the BET surface area (from 21 to 425 m^2/g) and mesopore volume (0.31 cm^3/g) after regeneration. XRD patterns of the regenerated catalyst (Figure S16) further confirm the full preservation of the MFI framework, with characteristic diffraction peaks matching those of the fresh sample. Additionally, SEM imaging (Figure S17) demonstrates that the Hier-Z5-43 particles retain their well-defined morphology and sharp edges after five cycles, with no evidence of fragmentation or surface cracking, confirming their mechanical durability under reaction and thermal stress. Furthermore, TG/DSC analysis of the spent catalyst (Figure S18) quantified the carbonaceous deposits (~7 wt%), identifying a mixture of soft coke (42% of total residue, combusting at ~360 °C) and more graphitized hard coke (58%, ~415 °C). Complementary FT-IR analysis (Figure S19) reveals characteristic aromatic C=C and C=O vibrations (1600–1700 cm^{-1}), confirming that the deposits primarily consist of polycyclic aromatics and oxygenated intermediates. The relatively low total coke content and the ease of its oxidative removal represent critical attributes for practical deployment.

Upcycling of real-world plastic wastes. The practical utility of Hier-Z5-43 was rigorously tested using diverse real-world polyethylene waste streams, including bottle-derived LDPE and HDPE (Figure 6E & G). Detailed spectra (Figures S20–S23) confirm consistent aromatic distribution across bottle-derived feedstocks. Supplementary tests with 3 wt% additives reveal that Hier-Z5-43 is tolerant toward oxygenated species like BHT (~55% liquid yield), yet susceptible to nitrogen-containing contaminants (e.g., Antioxidant 3114) due to Brønsted acid site poisoning. This selective tolerance highlights the catalyst's versatility for common oxygenated waste, while necessitating pretreatment or modification for nitrogen-rich streams.

Accordingly, even with these inherent variations in crystallinity and additive content, all real-world feedstocks were efficiently converted, consistently yielded over 50 wt% liquids and ~40 wt% gases. Notably, the aromatic productivity for molded bottle plastics (34.8–36.7%) matched the high performance achieved with pure polymer powders, demonstrating the system's robustness against real-world complexity (Figure 6F). GC–MS analysis confirmed that C_8–C_{12} aromatics remained the dominant product class across all substrates (Figure 6G). The consistently low to moderate coke formation (2.3%–6.8%, Figure 6H) provides direct evidence for the mesopore-assisted turnover mechanism. By facilitating rapid diffusion of reactive intermediates, the hierarchical structure minimizes coke precursors residence time, enabling efficient processing of challenging waste streams.

Techno-economic and environmental impact assessment

A combined Techno-Economic Analysis (TEA) and Life Cycle Assessment (LCA) was conducted to quantify the commercial and environmental potential of this hydrogen-free upcycling strategy involving no added metal active sites, benchmarking it against conventional routes (Figure 7A). The proposed route involves LDPE pretreatment, catalytic depolymerization over Hier-Z5-43, and product separation. Process simulations were conducted using the Aspen Plus platform, employing the PENG–ROB equation of state and an RYield reactor calibrated with our experimental yields (Figure S24). To evaluate economic robustness, the annual catalyst replacement cost was modeled across varying daily loss rates (1–5%) and unit prices, revealing a cost range of $7.2 to $65 million (Figure S25), underscoring the importance of catalyst stability.

Energy consumption analysis, quantified in MJ/kg LDPE (Figure 7B), revealed a substantial energetic advantage for the hierarchical zeolite system. The total energy demand for the H_2-free catalytic upcycling process using Hier-Z5-43 is calculated to be 17.0 MJ/kg LDPE. This is 10.9 MJ/kg lower than the traditional fossil-based aromatics production route (27.9 MJ/kg).[13,66,67] The significant energy saving stems directly from the mild operating conditions (280 °C, H_2-free) enabled by the highly active and selective catalyst, avoiding the intense energy inputs required for high-temperature catalysis or hydrogen production. Strategic heat integration is incorporated into the process design (Figure S24 & Table S10) to further optimize energy efficiency. The high-temperature product stream preheats the incoming LDPE feedstock and reaction gas, thus minimizing external utility for reactor heating. A systematic sensitivity analysis of key operational variables (Figure S26) validates the energy performance robustness across industrial operating windows. Reaction temperature variations from 260 to 300 °C cause a gradual rise in total energy duty (13.7 to 24.0 MJ/kg-LDPE) due to increased

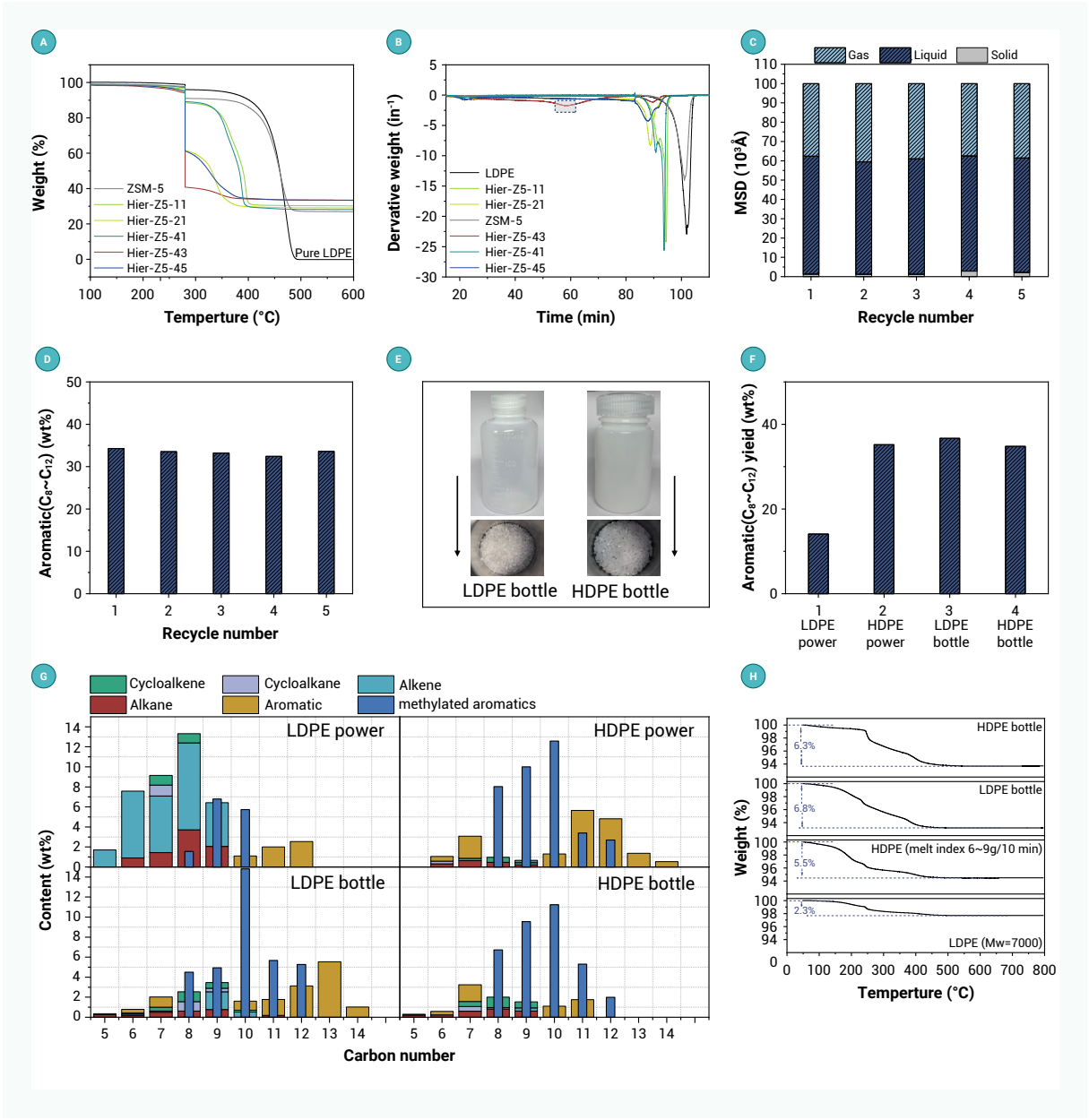

Figure 6. Stability, regenerability, and real-world waste upcycling. (A) TG and (B) DTG curves of LDPE decomposition over various catalysts at 280 °C. (C) Liquid, gas, and residue yield over five reaction-regeneration cycles using Hier-Z5-43. (D) C_8–C_{12} aromatic yield stability over five runs. (E) Product distribution and (F) C_8–C_{12} aromatic yields for real-world LDPE/HDPE powders and bottles. (G) Hydrocarbon type distribution for various real-world feedstocks. (H) TG analysis of spent catalysts showing coke deposition levels.

sensible heat for high-temperature gas-phase cracking, while pressure adjustments from 1 to 4 MPa induce a moderate increase (14.9 to 17.8 MJ/kg-LDPE) from extra compression work for N_2 pressurization and feedstock transport. Notably, the optimized baseline condition (280 °C, 3 MPa) achieves an ideal balance between reaction kinetics and energy efficiency, ensuring the total energy duty remains highly competitive relative to conventional fossil-based routes across the evaluated operating range. While incineration remains a net energy producer (-5 MJ/kg), it forfeits all molecular carbon value. Sensitivity analysis (Figure S27) confirms a baseline MSP of $1,684/ton, well below the market price (~$2,200/ton). Even with lower real-world yields (15–20 wt%), which increase the MSP to $3,200–$4,266/ton, the process remains viable through potential carbon credits or subsidies.

The LCA focused on the GWP, measured in kg CO_2 eq per kg of LDPE processed (Figure 7C). Based on a cradle-to-gate boundary (Figure S28) and mass-based allocation, the environmental impact of the hydrogen-free upcycling route was evaluated. This process demonstrates a highly favorable environmental profile, achieving a total GWP of 1255 kg CO_2 eq. Compared to conventional hydrocracking (Table S11), which requires substantial hydrogen input (30–50 kg/t) and higher energy intensity (3.5–5.5 MJ/kg), our approach offers a more sustainable pathway by eliminating hydrogen-associated emissions and reducing operational complexity. This represents a >55% reduction compared to both the fossil-based route (~2903 kg CO_2 eq) and incineration (~3127 kg CO_2 eq). Our system's GWP is also highly competitive with other advanced plastic conversion technologies reported in the literature.[13,17,50,67] This drastically lowered carbon footprint is a direct consequence of the process's dual advantage, i.e., avoiding emissions from virgin fossil feedstock production and minimizing its own operational energy intensity through catalytic efficiency.

In conclusion, the Hier-Z5-43 catalyst not only exhibits robust stability and real-world versatility but also enables an upcycling process that is substantially more energy-efficient and climate-friendly than current benchmarks. This holistic assessment confirms that synergistically optimizing pore structure and acidity translates into tangible system-level benefits for sustainable plastic waste valorization.

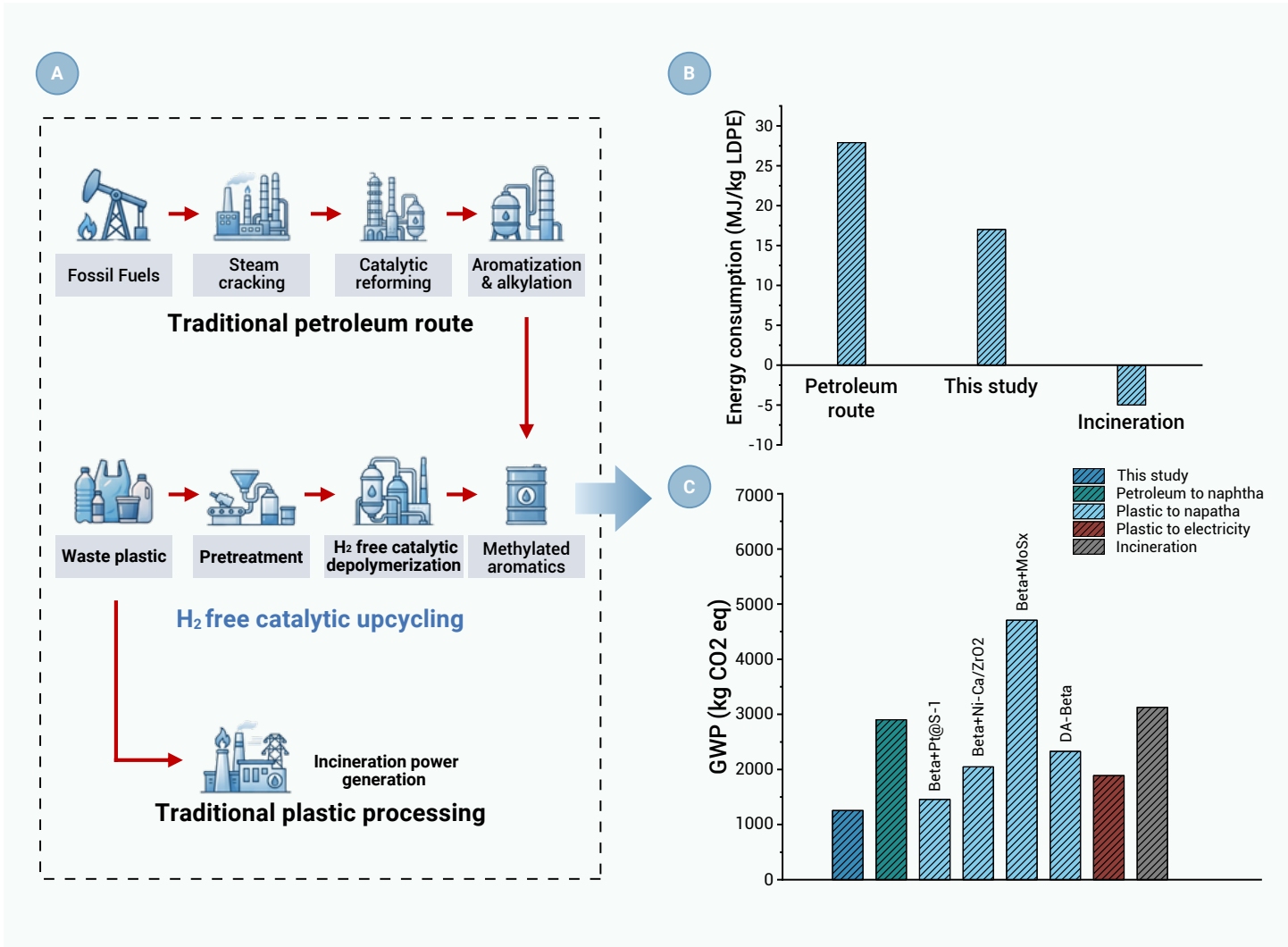

Figure 7. Techno-Economic and Environmental Assessment of H_2-Free Polyethylene Upcycling. (A) Comparative process routes for aromatics production and plastic waste management. (B)Energy consumption analysis (MJ/kg LDPE) of H_2-free catalytic upcycling versus the traditional petroleum route and incineration. (C) GWP assessment (kg CO_2 eq) comparing the catalytic upcycling process with conventional chemical and disposal methods.

CONCLUSIONS

This study demonstrates a highly efficient, hydrogen-free strategy for upcycling waste PE into high-value C_8–C_{12} methylated aromatics over hierarchical ZSM-5 with no added metal active sites. The key advance is the precise engineering of hierarchical ZSM-5 zeolite, where a synergistic balance between mesoporosity and Brønsted acidity (optimal at V_{meso}/V_{micro} ~2.73 and BAS density ~226 μmol/g) overcomes the diffusion limitations of conventional zeolites. *In-situ* spectroscopy and molecular dynamics simulations reveal that the optimized ~4.9 nm mesopores facilitated a synergy-driven cascade mechanism, accelerating the diffusion of key C10 intermediates by an order of magnitude to prevent over-cracking. This synergy enables the optimized catalyst (Hier-Z5-43) to achieve a peak C_8–C_{12} aromatic yield of 37.4% at mild 280 °C, outperforming several state-of-the-art metal-modified benchmarks. Beyond its performance with pure polymers, Hier-Z5-43 demonstrated exceptional robustness and versatility in upcycling real-world plastic waste, maintaining stable aromatic productivity over multiple regeneration cycles with manageable coke deposition. Furthermore, TEA and LCA assessments confirm that our process is both energetically efficient (17.0 MJ/kg) and environmentally superior, with a significantly reduced Global Warming Potential (1255 kg CO_2 eq) compared to conventional fossil-based routes. This work establishes a quantitative predictive design paradigm based on the V_{meso}/V_{micro} ratio for balancing mass transport and acidity in zeolite catalysts. This paradigm is generalizable to other bulky polyolefin feedstocks, providing a foundational design principle for polyolefin valorization and paving a sustainable path for the circular carbon economy.

REFERENCES

1. Ellis L.D., Rorrer N.A., Sullivan K.P., et al. (2021). Chemical and biological catalysis for plastics recycling and upcycling. *Nat. Catal.* **4**:539–556. DOI:10.1038/s41929-021-00648-4
2. Jehanno C., Alty J.W., Roosen M., et al. (2022). Critical advances and future opportunities in upcycling commodity polymers. *Nature* **603**:803–814. DOI:10.1038/s41586-021-04350-0
3. Tang Y. (2017). Efficient and selective degradation of polyethylenes into liquid fuels and waxes under mild conditions. *Sci. Adv.* 2. DOI: 10.1126/sciadv.1501591
4. MacLeo M., Arp H.P.H., Tekman M.B. and Jahnke A. (2021). The global threat from plastic pollution. *Science* **373**:61–65. DOI:10.1126/science.abg5433
5. Chamas A., Moon H., Zheng J., et al. (2020). Degradation rates of plastics in the environment. *ACS Sustain. Chem. Eng.* **8**:3494–3511. DOI:10.1021/acssuschemeng.9b06635
6. Hu K., Yang Y., Wang Y., et al. (2022). Catalytic carbon and hydrogen cycles in plastics chemistry. *Chem Catal.* **2**:724–761. DOI:10.1016/j.checat.2022.02.003
7. Vollmer I., Jenks M.J.F., Roelands M.C.P., et al. (2020). Beyond mechanical recycling: Giving new life to plastic waste. *Angew. Chem. Int. Ed.* **59**:15402–15423. DOI:10.1002/anie.201915651
8. Yu Z., Fan Y. and Lin F. (2025). Base-metal heterogeneous catalysts for upgrading plastics to light olefins. *Research* **8**:0731. DOI:10.34133/research.0731
9. Korley L.T.J., Epps T.H., Helms B.A. and Ryan A.J. (2021). Toward polymer upcycling-adding value and tackling circularity. *Science* **373**:66–69. DOI:10.1126/science.abg4503
10. Shi Y., Diao X., Ji N., et al. (2024). Advances and challenges for catalytic recycling and upgrading of real-world mixed plastic waste. *ACS Catal.* **15**:841–868. DOI:10.1021/acscatal.4c06344
11. Chin M.T. and Diao T. (2024). Industrial and laboratory technologies for the chemical

recycling of plastic waste. *ACS Catal.* **14**:12437–12453. DOI:10.1021/acscatal.4c03194
12. Yan J., Li G., Lei Z., et al. (2025). Upcycling polyolefins to methane-free liquid fuel by a Ru1-ZrO2 catalyst. *Nat. Commun.* **16**:2800. DOI:10.1038/s41467-025-57998-x
13. Li L., Luo H., Shao Z., et al. (2023). Converting plastic wastes to naphtha for closing the plastic loop. *J. Am. Chem. Soc.* **145**:1847–1854. DOI:10.1021/jacs.2c11407
14. Zhou Q., Wang D., Wang Q., et al. (2023). Mechanistic understanding of efficient polyethylene hydrocracking over two-dimensional platinum-anchored tungsten trioxide. *Angew. Chem. Int. Ed.* **62**:e202305644. DOI:10.1002/anie.202305644
15. Cen Z., Han X., Lin L., et al. (2024). Upcycling of polyethylene to gasoline through a self-supplied hydrogen strategy in a layered self-pillared zeolite. *Nat. Chem.* **16**:871–880. DOI:10.1038/s41557-024-01506-z
16. Chen S., Tennakoon A., You K.-E., et al. (2023). Ultrasmall amorphous zirconia nanoparticles catalyse polyolefin hydrogenolysis. *Nat. Catal.* **6**:161–173. DOI:10.1038/s41929-023-00910-x
17. Qiu Z., Lin S., Chen Z., et al. (2023). A reusable, impurity-tolerant and noble metal-free catalyst for hydrocracking of waste polyolefins. *Sci. Adv.* 9. DOI:10.1126/sciadv.adg5332
18. Ran H., Zhang S., Ni W. and Jing Y. (2024). Precise activation of C-C bonds for recycling and upcycling of plastics. *Chem. Sci.* **15**:795–831. DOI:10.1039/D3SC05701A
19. Chu M., Wang X., Wang X., et al. (2023). Site-selective polyolefin hydrogenolysis on atomic Ru for methanation suppression and liquid fuel production. *Research* **6**:0032. DOI:10.34133/research.0032
20. Gao R., Mao S., Lu B., et al. (2025). Efficient upcycling of polyolefin waste to light aromatics via coupling C—C scission and carbonylation. *Angew. Chem. Int. Ed.* **64**:e202424334. DOI:10.1002/anie.202424334
21. Lebreton L. and Andrady A. (2019). Future scenarios of global plastic waste generation and disposal. *Palgrave Commun.* **5**:6. DOI:10.1057/s41599-018-0212-7
22. Li H., Wu J., Jiang Z., et al. (2023). Hydroformylation of pyrolysis oils to aldehydes and alcohols from polyolefin waste. *Science* **381**:660–665. DOI:10.1126/science.adh1853
23. Li S., Li Z., Zhang F. and Chen J. (2024). Upgrading waste plastics to value-added aromatics. *Chem Catal.* **4**:100928. DOI:10.1016/j.checat.2024.100928
24. Hancock J.N. and Rorrer J.E. (2023). Hydrogen-free catalytic depolymerization of waste polyolefins at mild temperatures. *Appl. Catal. B: Environ. Energy* **338**:123071. DOI:10.1016/j.apcatb.2023.123071
25. Kwon T., Kim J. and Ro I. (2025). Hydrogen-free catalytic strategies for the upcycling of polyolefin plastics. *Korean J. Chem. Eng.* **43**:109–164. DOI:10.1007/s11814-025-00535-9
26. Cui Y., Xu Y., Zhang X. and Li Z. (2024). Sustainable aviation fuel: Biomass fostered future aviation. *Innov. Energy* **1**:100007. DOI:10.59717/j.xinn-energy.2024.100007
27. Duan J., Wang H., Li H., et al. (2023). Selective conversion of polyethylene wastes to methylated aromatics through cascade catalysis. *EES Catal.* **1**:529–538. DOI:10.1039/D3EY00011G
28. Fang Z., Wen C., Zhang X., et al. (2025). Advance, challenge, and outlook of carbon-increasing strategies for producing sustainable high-energy-density jet fuels from lignocellulosic derivatives. *Innov. Energy* **2**:100093. DOI:10.59717/j.xinn-energy.2025.100093
29. Mukhopadhyay R. and Kunzru D. (1993). Catalytic pyrolysis of naphtha on calcium aluminate catalysts - effect of potassium carbonate impregnation. *Ind. Eng. Chem. Res.* **32**:1914–1920. DOI:10.1021/ie00021a015
30. Qian K., Tian W., Yin L., et al. (2023). Aromatic production from high-density polyethylene over zinc promoted HZSM-5. *Appl. Catal. B: Environ. Energy* **339**:123159. DOI:10.1016/j.apcatb.2023.123159
31. Costa C.S., Thi H.D., Van Geem K.M. and Ribeiro M.R. (2022). Assessment of acidity and the zeolite porous structure on hydrocracking of HDPE. *Sustain. Energy Fuels* **6**:3611–3625. DOI:10.1039/D2SE00497F
32. Tang H., Li M., Chen D., et al. (2025). One-step production of isoalkane-rich sustainable aviation fuel fractions via catalytic pyrolysis of low-density polyethylene over Y-type zeolite. *ACS Sustain. Chem. Eng.* **13**:876–8772. DOI:10.1021/acssuschemeng.5c02722
33. Zhang F., Zeng M., Yappert R.D., et al. (2020). Polyethylene upcycling to long-chain alkylaromatics by tandem hydrogenolysis/aromatization. *Science* **370**:437–441. DOI:10.1126/science.abc544
34. Chen Z., Qiu Z., Lin S. and Lin B. (2025). Methanol-facilitated cascaded polyolefin upcycling enabling the efficient generation of high-value C9+ alkylaromatics. *Angew. Chem. Int. Ed.* **64**:e202503355. DOI:10.1002/anie.202503355
35. Du J., Zeng L., Yan T., et al. (2023). Efficient solvent- and hydrogen-free upcycling of high-density polyethylene into separable cyclic hydrocarbons. *Nat. Nanotechnol.* **18**:772–779. DOI:10.1038/s41565-023-01429-9
36. Han X., Zhang J., Qu Z., et al. (2025). Engineering noble metal-free nickel catalysts for highly efficient liquid fuel production from waste polyolefins under mild conditions. *Fuel* **382**:133733. DOI:10.1016/j.fuel.2024.133733
37. Vance B.C., Yuliu Z., Najmi S., et al. (2024). Unlocking naphtha from polyolefins using Ni-based hydrocracking catalysts. *Chem. Eng. J.* **487**:150468. DOI:10.1016/j.cej.2024.150468
38. Sun B., Xu H., Li T., et al. (2025). Hydrogen-free upcycling of polyethylene waste to methylated aromatics over Ni/ZSM-5 under mild conditions. *J. Hazard. Mater.* **482**:136564. DOI:10.1016/j.jhazmat.2024.136564
39. Zhan J., Li L., Dai R., et al. (2025). Engineering porous Beta zeolite-encapsulated nickel catalyst for waste polyolefins upcycling. *Appl. Catal. B: Environ. Energy* **373**:125359. DOI:10.1016/j.apcatb.2025.125359
40. Lee W.-T., van Muyden A., Bobbink F.D., et al. (2022). Mechanistic classification and benchmarking of polyolefin depolymerization over silica-alumina-based catalysts. *Nat. Commun.* **13**:4850. DOI:10.1038/s41467-022-32563-y
41. Gounder R. and Iglesia E. (2013). The catalytic diversity of zeolites: confinement and solvation effects within voids of molecular dimensions. *Chem. Commun.* **49**:3491–3509. DOI:10.1039/C3CC40731D
42. Sastre G. and Corma A. (2009). The confinement effect in zeolites. *J. Mol. Catal. A: Chem.* **305**:3–7. DOI:10.1016/j.molcata.2008.10.042
43. Wu X., Tennakoon A., Yappert R., et al. (2022). Size-controlled nanoparticles embedded in a mesoporous architecture leading to efficient and selective hydrogenolysis of polyolefins. *J. Am. Chem. Soc.* **144**:5323–5334. DOI:10.1021/jacs.1c11694
44. Tsubota S., Kokuryo S., Miyake K., et al. (2024). Understanding the role of the surface acidity of MFI zeolites during LDPE cracking: Decomposition temperature and product distribution. *ACS Catal.* **14**:18145–18155. DOI:10.1021/acscatal.4c06190
45. Wang Z., Gao L., Zhong X., et al. (2025). Accurately tuning the pore size and acidity of mesoporous zeolites for enhancing the catalytic hydrocracking of polypropylene. *J. Mater. Chem. A* **13**:2875–2883. DOI:10.1039/D4TA07329K
46. Tarach K.A., Pyra K., Siles S., et al. (2019). Operando study reveals the superior cracking activity and stability of hierarchical ZSM-5 catalyst for the cracking of low-density polyethylene. *ChemSusChem* **12**:633–638. DOI:10.1002/cssc.201802190
47. Hong W., Ahn J., Shin J.W., et al. (2025). Polyethylene hydrogenolysis over Ru supported on mesoporous MFI zeolite: Effects of mesoporosity and external acid sites. *ACS Catal.* **15**:10578–10590. DOI:10.1021/acscatal.5c00032
48. Tan J.Z., Ortega M., Miller S.A., et al. (2024). Catalytic consequences of hierarchical pore architectures within MFI and FAU zeolites for polyethylene conversion. *ACS Catal.* **14**:7536–7552. DOI:10.1021/acscatal.4c01213
49. Tan J.Z., Hullfish C.W., Zheng Y., et al. (2023). Conversion of polyethylene waste to short chain hydrocarbons under mild temperature and hydrogen pressure with metal-free and metal-loaded MFI zeolites. *Appl. Catal. B: Environ. Energy* **338**:123028. DOI:10.1016/j.apcatb.2023.123028
50. Azam M.U., Fernandes A., Ferreira M.J. and Graca I. (2024). Pore-structure engineering of hierarchical β zeolites for the enhanced hydrocracking of waste plastics to liquid fuels. *ACS Catal.* **14**:16148–16165. DOI:10.1021/acscatal.4c05354
51. Zhou X., Han X., Qu Z., et al. (2024). Hierarchical FAU zeolites boosting the hydrocracking of polyolefin waste into liquid fuels. *ACS Sustain. Chem. Eng.* **12**:6013–6022. DOI:10.1021/acssuschemeng.4c01097
52. Xu W., Huang Y., Lin Z., et al. (2025). Bayesian optimization of hierarchical ZSM-5 for high-efficiency polyolefin waste recycling to light olefins. *ACS Catal.* **15**:20926–20938. DOI:10.1021/acscatal.5c06271
53. Ruan Q., Xia H., Yuan Z., et al. (2025). Decoupling acidity from micropore confinement in an amorphous–crystalline composite for selective polyolefin waste cracking. *J. Am. Chem. Soc.* **148**:474–482. DOI:10.1021/jacs.5c14336
54. Duan J., Chen W., Wang C., et al. (2022). Coking-resistant polyethylene upcycling modulated by zeolite micropore diffusion. *J. Am. Chem. Soc.* **144**:14269–14277. DOI:10.1021/jacs.2c05125
55. Feng J., Duan J., Hung C.-T., et al. (2024). Micelles cascade assembly to tandem porous catalyst for waste plastics upcycling. *Angew. Chem. Int. Ed.* **63**:e202405252. DOI:10.1002/anie.202405252
56. Lee S., Park Y. and Choi M. (2024). Cooperative interplay of micropores/mesopores of hierarchical zeolite in chemical production. *ACS Catal.* **14**:2031–2048. DOI:10.1021/acscatal.3c05170
57. Christensen C.H., Johannsen K., Törnqvist E., et al. (2007). Mesoporous zeolite single crystal catalysts: Diffusion and catalysis in hierarchical zeolites. *Catal. Today* **128**:117–122. DOI:10.1016/j.cattod.2007.06.082
58. Thommes M., Kaneko K., Neimark A.V., et al. (2015). Physisorption of gases, with special reference to the evaluation of surface area and pore size distribution (IUPAC Technical Report). *Pure Appl. Chem.* **87**:1051–1069. DOI:10.1515/pac-2014-1117
59. Rejman S., Reverdy Z.M., Bör Z., et al. (2025). External acidity as performance descriptor in polyolefin cracking using zeolite-based materials. *Nat. Commun.* **16**:2980. DOI:10.1038/s41467-025-57158-1
60. Hullfish C.W., Tan J.Z., Adawi H.I. and Sarazen M.L. (2023). Toward intrinsic catalytic rates and selectivities of zeolites in the presence of limiting diffusion and deactivation. *ACS Catal.* **13**:13140–13150. DOI:10.1021/acscatal.3c03559
61. Gulmine J., Janissek P., Heise H. and Akcelrud L. (2002). Polyethylene characterization by FTIR. *Polym. Test.* **21**:557–563. DOI:10.1016/S0142-9418(01)00124-6
62. Zhou Q., Wang D., Wang Q., et al. (2023). Mechanistic understanding of efficient polyethylene hydrocracking over two-dimensional platinum-anchored tungsten trioxide. *Angew. Chem. Int. Ed.* **62**:e202305644. DOI:10.1016/S0142-9418(01)00124-6
63. Wang S., Wang W., Chu M., et al. (2024). Ultra-narrow alkane product distribution in polyethylene waste hydrocracking by zeolite micro-mesopore diffusion optimization. *Angew. Chem. Int. Ed.* **63**:e202409288. DOI:10.1002/anie.202409288

64. Wang W., Wang S., Li W., et al. (2025). Coordinating cracking and hydrogenation of polyethylene waste via acid-metal site isolation for selective hydrocarbon production. *Chem. Eng. Sci.* **315**:121882. DOI:10.1016/j.ces.2025.121882
65. Bu L., Nimlos M.R., Robichaud D.J., et al. (2018). Diffusion of aromatic hydrocarbons in hierarchical mesoporous H-ZSM-5 zeolite. *Catal. Today* **312**:73–81. DOI:10.1016/j.cattod.2018.02.012
66. Zhao Z., Chong K., Jiang J., et al. (2018). Low-carbon roadmap of chemical production: A case study of ethylene in China. *Renew. Sustain. Energy Rev.* **97**:580–591. DOI:10.1016/j.rser.2018.08.008
67. Luo H., Li L., Sun T., et al. (2025). Green upcycling of waste agricultural plastic film under mild conditions. *CCS Chem.* **7**:3185–3195. DOI:10.31635/ccschem.025.202404851

FUNDING AND ACKNOWLEDGMENTS

The authors would like to acknowledge financial support from the National Key R&D Program of China (2024YFB4206204), the National Natural Science Foundation of China (Grant No. 52376213, and 52006196), Key R&D Program of Zhejiang (2025C01173&2024C03225) and the Fundamental Research Funds for the Central Universities (Grant No. 2022ZFJH004)

AUTHOR CONTRIBUTIONS

Bingyan Sun: Writing – Original Draft, Conceptualization, Investigation, Methodology, Data Curation. Bo Li: Software, Formal Analysis. Mate Marc: Methodology, Visualization. Linjia Yin: Software, Data Curation. Qihui Song: Formal Analysis, Validation Xiaopeng Shi: Investigation, Visualization Dingran Wang: Methodology, Visualization Fawei Lin: Writing – Review & Editing, Visualization, Validation, Supervision. Kaige Wang: Writing – Review & Editing, Funding Acquisition, Project Administration, Resources, Supervision. All authors contributed to the manuscript and approved the final version.

DECLARATION OF INTERESTS

The authors declare no competing interests.

DATA AND CODE AVAILABILITY

Data are available from the corresponding author upon reasonable request.

SUPPLEMENTAL INFORMATION

It can be found online at: https://doi.org/10.59717/j.xinn-energy.2026.100155